Solid State Ionics 241 (2013) 36–45

Contents lists available at SciVerse ScienceDirect

Solid State Ionics

journal homepage: www.elsevier.com/locate/ssi

Influence of chromium content on the optical and electrical properties of $Li_{1+x}Cr_xTi_{2-x}(PO_4)_3$

M. Pérez-Estébanez [a], J. Isasi-Marín [a], C. Díaz-Guerra [b], A. Rivera-Calzada [c,*], C. León [c], J. Santamaría [c]

[a] Departamento de Química Inorgánica I, Universidad Complutense de Madrid, Ciudad Universitaria s/n, 28040, Madrid, Spain
[b] Departamento de Física de Materiales, Universidad Complutense de Madrid, Ciudad Universitaria s/n, 28040, Madrid, Spain
[c] Departamento de Física Aplicada III, Universidad Complutense de Madrid, Ciudad Universitaria s/n, 28040, Madrid, Spain

ARTICLE INFO

Article history:
Received 28 September 2012
Received in revised form 5 February 2013
Accepted 2 April 2013
Available online 2 May 2013

Keywords:
Ionic transport
Lithium ionic conductors
Solid electrolytes
Lithium batteries

ABSTRACT

Optical and electrical properties of samples with $Li_{1+x}Cr_xTi_{2-x}(PO_4)_3$ composition ($x = 0$, 0.05 and 0.1) prepared by a low temperature sol-gel method have been investigated. XRD and Raman spectroscopy measurements respectively reveal the rhombohedral-Nasicon structure of the grown samples and a disorder of Li^+ ions with increasing chromium content. Electrical properties were studied by impedance spectroscopy and both dc and grain boundary ionic conductivity increase with Cr content. A high ionic conductivity value of $1.4 \cdot 10^{-4}$ S cm^{-1} at room temperature and an activation energy of 0.31 eV have been obtained for $x = 0.1$, which are comparable to those measured in the best ionic conductors reported to date. Photoluminescence and cathodoluminescence spectra indicate that self-trapped excitons and oxygen defects related to the TiO_6 octahedra structural units are responsible for the observed luminescence in the visible spectral range, explaining the possible electronic origin of a residual conductivity measured in all the samples. Cr incorporation gives rise to infrared emission bands, attributed to different Cr^{3+} and Ti^{3+} intraionic transitions, that may be related to the better grain connectivity achieved by Cr doping.

1. Introduction

Lithium based solid electrolytes have been extensively studied for their application in high energy density batteries and fuel cells [1,2]. $LiTi_2(PO_4)_3$ and their derivatives are one of the best candidates, because the smaller ionic radius of the Ti^{4+}, as compared to other tetravalent cations, fits with the size of the Li ion, yielding an enhanced Li ion diffusivity [3–9]. The crystal structure of $LiTi_2(PO_4)_3$ (LTP) is based in the NASICON rhombohedral structure ($R\bar{3}c$ space group) and can be described as formed by infinite ribbons of $[Ti_2(PO_4)_3]^-$ units with [102] orientation formed by corner-sharing $[TiO_6]$ octahedra and $[PO_4]$ tetrahedra. Li^+ cations may occupy two interstitial positions within this network, the so-called M1 site (one per formula unit, crystallographic position 6b) and the M2 sites (three per formula unit, crystallographic positions 18e). The M1 site is six-fold coordinated with the oxygen atoms and the M2 site has an eight-fold coordination. Both sites alternate along the channels which form a three-dimensional network. In the $LiTi_2(PO_4)_3$ compound, Li^+ ions occupy preferentially the low connectivity M1 positions [10]. Although the starting material $LiTi_2(PO_4)_3$ shows moderate lithium conductivity, the appropriate substitution of Ti^{4+} with trivalent metals like Al^{3+}, Fe^{3+} or Cr^{3+} improves the electrical properties as it was systematically shown for the first time by Aono et al. [11,12]. These authors reported that the increase of ionic conductivity observed in $Li_{1+x}M^{3+}{}_xTi_{2-x}(PO_4)_3$ compounds was due both to the increase of the lithium content and to a better connectivity of the grains caused by a density increase associated to segregated phases in grain boundaries acting as binders. This is probably the origin of the high ionic conductivity of almost 10^{-3} S cm^{-1} at room temperature [13] found for $Li_{1.3}Al_{0.3}Ti_{1.7}(PO_4)_3$. Since its finding, many studies have focused on the determination of the conduction mechanisms in bulk and grain boundaries in these Al-substituted materials [14–18] and also on their synthesis by alternative methods aimed to reduce grain boundary resistance [19–22].

Grain boundary connectivity, which plays a crucial role in the application of this family of compounds, is not a well-understood process and, in fact, secondary phases could cause a stoichiometry imbalance in the bulk of the grains which may yield unwanted electronic conductivity. Moreover, the properties of the NASICON-type Li^+ conductor compounds critically depend on the Lithium stoichiometry and possible lithium losses associated to high temperature ceramic methods [18]. In this paper, we examine these concerns in the less explored $Li_{1+x}Cr_xTi_{2-x}(PO_4)_3$ compound via soft synthesis. Samples with high Cr doping ($x = 0.3$–0.8) synthesized by solid state chemistry are known to produce samples with a highly porous microstructure, improving sample densification with Cr content but causing phase segregation at grain boundaries [23]. In our approach, we have synthesized $Li_{1+x}Cr_xTi_{2-x}(PO_4)_3$ in the low doping level range ($x = 0$, 0.05 and 0.1) via a sol-gel synthesis route to minimize synthesis temperature and possible lithium losses. Dielectric

* Corresponding author at: Universidad Complutense de Madrid, 28040 Madrid, Spain. Tel.: +34 91 394 44 35; fax: +34 91 394 51 96.
E-mail address: alberto.rivera@fis.ucm.es (A. Rivera-Calzada).

0167-2738/$ – see front matter © 2013 Elsevier B.V. All rights reserved.
http://dx.doi.org/10.1016/j.ssi.2013.04.001

spectroscopy shows the characteristic ionic conductivity of the material and a residual value at the lowest frequencies. A set of complementary structural characterization techniques; field emission scanning electron microscopy (FESEM), X-ray diffraction (XRD) and Raman spectroscopy, as well as luminescence spectroscopies and transport measurements (dielectric spectroscopy) were used in order to investigate defects that can affect bulk and grain boundary dynamics.

2. Experimental

$Li_{1+x}Cr_xTi_{2-x}(PO_4)_3$ compounds with $x = 0$, 0.05 and 0.1 were prepared by the Pechini method [24] using Li_2NO_3, $Cr(NO_3)_3 \cdot 9H_2O$, $NH_4H_2PO_4$ and $TiC_8H_{24}O_4$ as starting materials. Citric acid (CA) and ethylene glycol (EG) were added as complexing and polymer agents respectively. $TiC_8H_{24}O_4$ was added to a saturated solution of CA whose pH was previously adjusted to 8 to promote ionization and complexation of titanium. After total dissolution, the rest of the reactants were added to the solution. Then, the appropriate amount of EG was mixed and the temperature was increased to 140 °C to promote polyesterification between CA-complexes and EG. During heating, solutions became more viscous until a polymeric gel was formed. The obtained gel was aged in air at room temperature during four days and subsequently heated up to 350 °C until a dark powder precursor was obtained. The powder precursors were heated in air at 750 °C during 4 h to obtain compounds of composition $Li_{1+x}Cr_xTi_{2-x}(PO_4)_3$ with $x = 0$, 0.05 and 0.1. The nanometric particles obtained (60–200 nm) were cold pressed at 150 MPa and annealed at 1000 °C to increase compaction and improve the electrical grain boundary, resulting in sub-micron grains. In order to compare the structure and properties of our samples with those grown by the conventional solid state reactions [12,25,26], an additional $Li_1Ti_2(PO_4)_3$ sample was grown following the same procedure but using a synthesis temperature of 800 °C. Chemical analyses were carried out by Inductive Coupled Plasma-Atomic Emission Spectroscopy (ICP-OES) using a Perkin Elmer Optima 3300 DV analyzer both before and after annealing at 1000 °C, in order to determine the lithium content. Analysis results are in good agreement with stoichiometry. Annealing did not yield to significant variations in atomic composition and no evidence of lithium loss was found.

XRD patterns of the synthesized powders and pellets were collected on a Philips X'Pert PRO MPD instrument using $CuK\alpha_1$ radiation. A step scan of 0.033° (2θ) in the range 10–120° and a counting time of 0.4 s for each step were employed. The instrumental parameters were previously calibrated using the LaB_6 standard NIST SRM 660b. Powder diffraction data were refined by the Rietveld method using the FullProf software [27] and a Thompson Cox function to describe the peak shape. The morphological characterization of powders and pellets were performed by field emission scanning electron microscopy (FESEM), using a JEOL-6335F microscope working at 10 kV.

The electrical properties of the compacts, typically 13 mm diameter and 1 mm thickness, were analyzed by impedance spectroscopy. Measurements were carried out in a BDS80 Broadband Dielectric Spectroscopy system (Novocontrol). The sample response was obtained from an Alpha Analyzer in the frequency range of 10^{-2}–10^7 Hz and temperature range 123 to 523 K within ± 0.1 K temperature variation during measurement. 1 V voltage signal was applied to the sample, and silver paste was used to define the electrodes on the sample, which was kept under N_2 flow in the system cryostat during measurements.

Micro-Raman and photoluminescence (PL) measurements were carried out at room temperature in a Horiba Jovin-Ybon LabRAM HR800 system. The samples were excited by a 325 nm He–Cd laser on an Olympus BX 41 confocal microscope with a 40× objective. A charge coupled device (CCD) detector was used to collect the scattered light dispersed by a 2400 lines/mm grating. Cathodoluminescence (CL) measurements were carried out in a Hitachi S-2500 scanning electron microscope. Measurements were performed using an accelerating voltage of 20 kV at temperatures between 90 and 295 K. CL spectra in the UV-IR range (300–800 nm, equivalent to 4.14–1.55 eV) were recorded using a CCD camera with a built-in spectrograph (Hamamatsu PMA-111) and corrected for system response.

3. Results and discussion

3.1. X-ray diffraction

The crystal structure of materials of $Li_{1+x}Cr_xTi_{2-x}(PO_4)_3$ composition, with $x = 0$, 0.05 and 0.1, was studied by X-ray diffraction, both powders and pellets. All the diffraction patterns can be indexed to rhombohedral symmetry with space group $R\bar{3}c$ corresponding to a NASICON-type structure. Fig. 1 shows the XRD patterns of powder samples. Cell parameters, volume and agreement factors obtained by Rietveld refinement are presented in Table 1. Lithium atoms were assumed to occupy the M1 site (6b special position) and not included in the refinement due to their low X-ray scattering power. Small differences in cell parameters with the chromium content have been found in the studied compositional range, due to the similar atomic radii of Ti^{4+} (0.605 Å) and Cr^{3+} (0.615 Å) in octahedral coordination. In general, c increases with x, whereas the change in a is small and the c/a ratio keeps constant, in agreement with results reported by Lin et al. [23]. A systematic increase in a parameter with sintering treatment is observed which may be probably due to differences in lithium disposition within M1 and M2 cavities [14].

3.2. Study of particle size and morphology

FESEM studies show that the $Li_{1+x}Cr_xTi_{2-x}(PO_4)_3$ powder samples are formed by heterogeneous-sized agglomerates of small particles. The undoped powder sample, Fig. 2(a), is formed by individual particles of 100–200 nm in size. On the contrary, smaller particles, of about 60 nm, and spherical shape are found in the Cr-doped samples. Such particles are partially sintered, giving rise to larger grains, Fig. 2(c) and (e).

When powders were pressed and annealed, larger particles are found, as can be observed in Fig. 2(b), (d) and (f). The particle shape becomes prismatic and hexagonal faces can be clearly recognized in the undoped sample due to grain growth, while chromium-doped particles show irregular shape and lower size (600 nm against 800 nm in the undoped material). Density was determined from the weight and physical dimensions of the pellets and compared with theoretical density calculated from cell parameters. Relative density was found to increase with increasing chromium content: the undoped sample has a 50% of theoretical density while 53% and 60% were obtained from chromium-doped samples with x = 0.05 and 0.1 respectively. A decrease of porosity with chromium content has also been reported by Aono et al. [12]. Although it is well known that density can be increased by thermal treatments at higher temperatures and by the addition of binders, the aim of

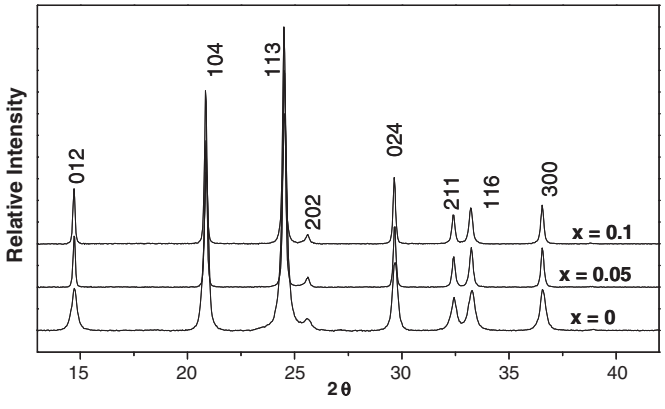

Fig. 1. XRD patterns of the powder samples.

Table 1
Cell parameters, volume, *c*/*a* ratio and agreement factors of the Rietveld refinements of powders and pellets.

		a (Å)	c(Å)	c/a	Vol(Å^3)	R_b	R_f
x = 0	Powder	8.5108(5)	20.8803(2)	2.45	1309.8(2)	2.77	1.87
	Pellet	8.5111(3)	20.8791(1)	2.45	1309.8(1)	4.89	3.72
x = 0.05	Powder	8.5102(3)	20.8838(1)	2.45	1309.8(9)	2.31	2.14
	Pellet	8.5141(5)	20.8821(1)	2.45	1310.9(1)	5.35	4.25
x = 0.1	Powder	8.5106(3)	20.8903(1)	2.45	1310.4(1)	3.07	1.94
	Pellet	8.5151(4)	20.8902(1)	2.45	1311.8(1)	3.53	4.38

this work is to minimize lithium losses and study the grain connectivity of the series without additives. Therefore, we avoided the addition of any phase acting as binder and used the lowest temperatures possible in order to prevent the loss of lithium and properly characterize the sintering mechanism and electrical behavior of $Li_{1+x}Cr_xTi_{2-x}(PO_4)_3$.

3.3. Impedance spectroscopy

We have investigated the ion dynamics by complex conductivity measurements of pellets of composition $Li_{1+x}Cr_xTi_{2-x}(PO_4)_3$ with x = 0, 0.05 and 0.1 after annealing at 1000 °C. Since the two Cr-doped samples show the same qualitative behavior, Fig. 3(a) shows the ionic conductivity versus frequency of $Li_{1.1}Cr_{0.1}Ti_{1.9}(PO_4)_3$ at different temperatures as a representative example. The typical features displayed by ion conductors can be clearly identified. In the lower temperature range, we observe the dispersive behavior of the bulk conductivity at the highest frequencies, with a power law frequency-dependent conductivity that originated in the correlated jumps of the lithium ions. By decreasing frequency, a *plateau* characteristic of the dc bulk conductivity (σ_{dc}) of the sample is expected. This *plateau* is not clearly observed in Fig. 3(a), since a long range or dc response cannot be fully developed within the grains as the grain size in the samples studied is only 600–800 nm. Nevertheless the value of σ_{dc} at each temperature can be extracted from the plots with the help of the dielectric modulus, a representation of the same data less sensitive to grain boundary blocking and simply related to the conductivity by:

$$M^* = \frac{1}{\varepsilon^*} = \frac{j\omega}{\sigma^*} \quad (1)$$

In Fig. 3(b) we present the imaginary part of the modulus M", in which the ionic transport shows up as a relaxation peak, whose

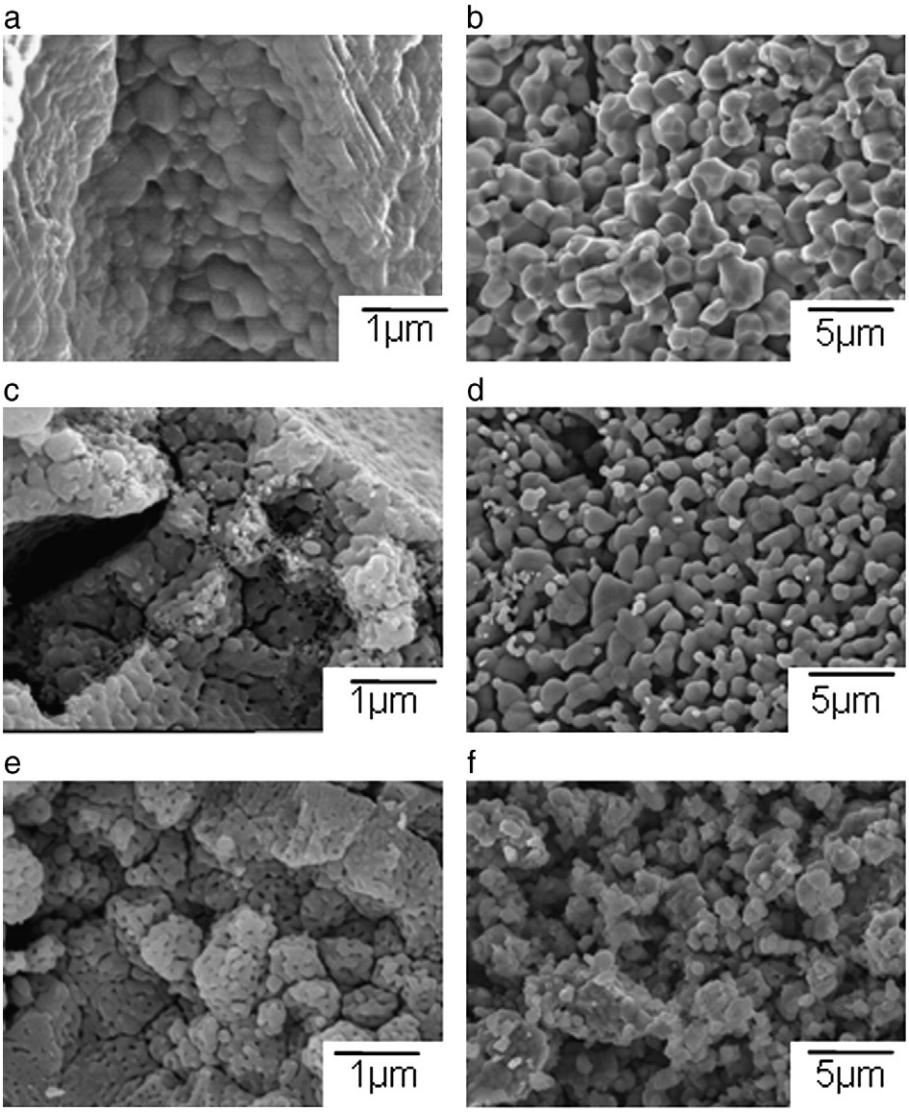

Fig. 2. SEM micrographs of $LiTi_2(PO_4)_3$ (a,b), $Li_{1.05}Cr_{0.05}Ti_{1.95}(PO_4)_3$ (c,d) and $Li_{1.1}Cr_{0.1}Ti_{1.9}(PO_4)_3$ (e,f) samples. Images (a), (c) and (e) correspond to the as-grown powders while figures (b), (d) and (f) correspond to the same materials after pressing and annealing at 1000 °C.

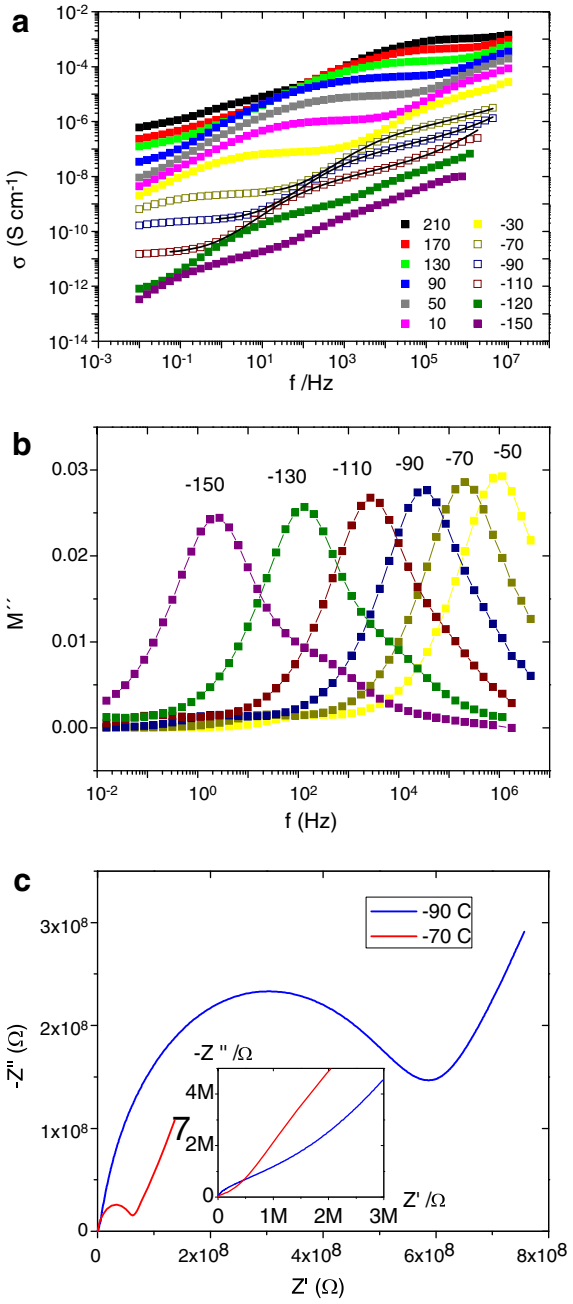

Fig. 3. (a) $Li_{1.1}Cr_{0.1}Ti_{1.9}(PO_4)_3$ ionic conductivity versus frequency at different temperatures in °C, as read in the legend. Lines are fits to extract dc and grain boundary conductivity (see text). (b) Spectra of the dielectric modulus, M" showing the dc conductivity relaxation. (c) Nyquist plot, −Z" vs Z', of the same sample at selected temperatures to show the grain boundary conductivity (main figure), and the bulk contribution (inset).

maximum is located at a frequency characteristic of the diffusion process, and yields the dc conductivity using the formula:

$$\sigma_{dc} = \varepsilon_\infty \varepsilon_0 2\pi f_M \tag{2}$$

being $\varepsilon_\infty\varepsilon_0$ the limiting value of the permittivity at the highest frequency, and f_M the frequency of the maximum of the imaginary part of the modulus [28]. The dc conductivity as well as the crossover frequency to the ac power law regime, increase with temperature in a thermally activated fashion. By further decreasing frequency or increasing temperature, a sudden decrease of the conductivity occurs, due to the blocking of ions at grain boundaries. A well-defined plateau yielding the grain boundary conductivity is observed crossing our experimental frequency window towards higher frequencies when increasing temperature. The grain boundary conductivity σ_{gb} is also thermally activated with a similar activation energy as for σ_{dc}. In general this contribution is composed by at least two components, pores and grain–grain interconnectivity, being the latter the dominant one regarding electrical behavior. The same features of the ionic conductivity can be analyzed in the Nyquist plot of the sample (−Z" vs Z'). Fig. 3(b) shows the curves at two selected temperatures in which we have in our frequency window the bulk and dc conductivity contributions. In this representation each one appears as a distorted semicircle, as observed in Fig. 3(b) for the case of the grain boundary relaxation (main figure). The inset shows the bulk or dc response, with incomplete semicircles due to the sub-micron size of the grains of the sample.

At lower frequencies and higher temperatures, there is another large decrease in the conductivity [Fig. 3(a)] due to the blocking of ionic carriers at the metallic electrodes. This effect is an indication of the ionic nature of the carriers in the material, since electrons are not blocked at silver electrodes, and evidences that the charge transport in the samples is mostly ionic. Finally, only visible for the highest temperatures, another plateau develops at the lowest frequencies, indicating the possible presence of a small electronic conductivity at a level below 10^{-6} S/cm. In fact these low levels of residual conduction are present in the undoped sample, as evidenced in Fig. 4(a), in which the electrical conductivity of LTP sample is plotted versus frequency. In this sample, charge dynamics is governed by ions giving rise to the strong increase of the real part of the permittivity ε' up to 10^8 (Fig. 4(b)), which is the typical increase in the capacitance of the ionic conducting samples when decreasing frequency at high temperatures due to the accumulation of ionic charge in the metallic contacts [29]. The residual contribution can be estimated from the conductivity data at the lowest frequency for the highest temperatures [Fig. 4(a)].

Fig. 5 shows the Arrhenius plot of de dc, grain boundary and "electronic" conductivities observed in the samples studied. The dc conductivity calculated from the modulus were double checked to test the uncertainty of the values by fitting the data with a two parallel R-CPE circuits connected in series with the commercially available software Zview. Fits are shown as lines in Fig. 3(a), and yield the same values for the dc and grain boundary conductivity within ±20% error. To completely cover the error in the determination of the dc values, overestimated error bars of ±30% are presented in the Arrhenius plot, but they fall within the size of the points in Fig. 5.

In all cases a thermally activated behavior is observed for the dc conductivity (lines in Fig. 5), and data can be accurately described with a single exponential term,

$$\sigma_{dc} = \sigma_\infty \exp(-E_a/kT) \tag{3}$$

being E_a the activation energy and σ_∞ the pre-exponential factor, which is customarily described in terms of the following expression:

$$\sigma_\infty = \frac{4\alpha e^2 a^2 \nu_0 N e^{S/k_B}}{k_B} \tag{4}$$

where α is a geometrical factor, a is the jump distance, ν_0 is the attempt frequency, N is the concentration of carriers, S is a configurational entropy term, e is the electron charge and k_B is Boltzmann's constant. Table 2 summarizes the activation energy, pre-exponential factor and ionic conductivity at room temperature in the bulk and grain boundaries obtained from Arrhenius fit. Since the structural parameters of all the samples are very similar and there is only a 10% difference in lithium concentration (1 versus 1.1 per formula unit), a similar σ_∞ term is found (Table 2).

From the fits of the dc conductivity data of Fig. 5 the activation energy of the bulk conductivity in the undoped sample is 0.67 eV.

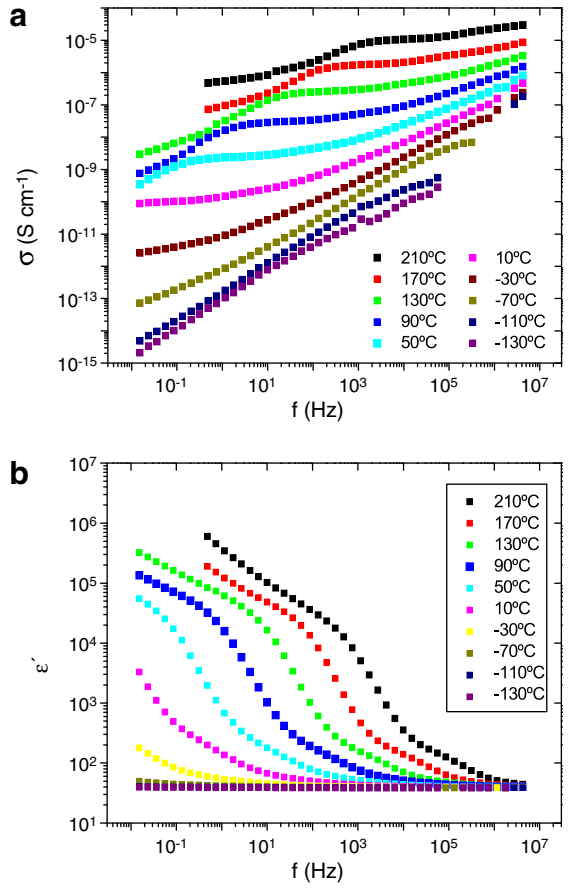

Fig. 4. (a) $LiTi_2(PO_4)_3$ ionic conductivity versus frequency at temperatures −130 to 210 °C from bottom to top, (b) spectra of the imaginary part of the permittivity ε' at the same temperatures, from left to right.

This value is higher than the 0.35 eV activation energy reported [14] for ceramic samples prepared at 950 °C, which can be attributed to the lower temperature synthesis used in the present work, (750 °C). Actually, we find out that an increase of only 50 °C is enough to recover the activation energy values reported in the literature, as we measured in the sample we prepared for this purpose. Instead of increasing synthesis temperature, we achieve the increase in the dc conductivity with the small addition of Cr. The same analysis is valid for the grain boundary conductivity, whose value is much lower than that found in ceramic samples [14].

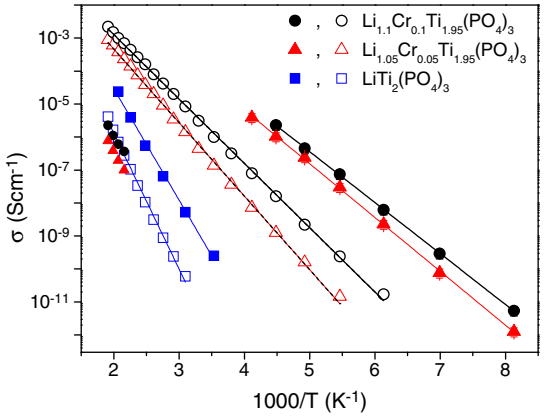

Fig. 5. DC conductivity (solid) and grain boundary (open) conductivity of the samples studied according to the legend. Lines are fits of the data to a thermally activated behavior (see text), and error bars of ±30% are plotted for the dc values. Small solid symbols are the electronic contribution of the samples estimated from the conductivity plots at the highest temperatures and the lowest frequency.

Focusing on the Cr doped compounds, dc activation energy decreases to 0.32–0.31 eV, a very similar value in agreement with the very same structural parameters of the samples obtained in the previous section. The decrease in the activation energy with Cr insertion can be rationalized as a consequence of the facilitation of favorable pathways for lithium motion [30,31]. As recent simulations have demonstrated, when lithium content is increased by doping with trivalent cations, part of the mobile lithium ions are transferred to the M2 positions which are high connectivity sites, leaving the same amount of vacancies in M1 bottlenecks [32]. Liberation of M1 bottleneck positions facilitates the ionic transport of lithium through the material as a low energy pathway is established along M1 and M2 sites.

The largest σ_{dc} is found in the most doped sample, showing conductivity values of 1.4 10^{-4} S/cm at room temperature. Note that these values are close to those of the fast ionic conductors (1 mS/cm at room temperature) [1,2,17,19,31,33,34].

A slightly different trend is observed for the grain boundary conductivity, the grain boundary (gb) activation energy decreases from 0.81 eV in the undoped sample to 0.44 and 0.39 eV when doping LTP wit Cr. The higher activation energy evidences a less effective grain connectivity in the undoped sample, which correlates with the differences in densification. Small particles in the initial powder in Cr-doped samples (Fig. 2) increase the total surface area in the compact and the driving force for densification during sintering is enhanced, improving the packing of the grains with increasing Cr content. On the other hand, we have no indication of nucleation of secondary phases at grain boundaries in this doping range upon sintering, which is reflected in the electrical connectivity. In fact, a minimum value of two orders of magnitude difference between dc and gb conductivity is found for the more doped Cr sample.

Also in Fig. 5, the tentatively "electronic" conductivity of the $LiTi_2(PO_4)_3$ sample is plotted together with the residual contribution found in the Cr doped samples. It is remarkable that a very similar value, within experimental error, is obtained in the Cr doped samples, in the same range as the gb conductivity of the undoped LTP sample. A rough estimation of the activation energy of the residual contribution gives 0.66 ± 0.05 eV, lower than the 0.8 eV of the LTP. We may speculate that a weak semiconducting behavior is present giving rise to a very low electronic conduction, around 4 orders of magnitude smaller than the ionic transport at 200C.

In the following, important issues that cannot be addressed by dielectric spectroscopy, such as disorder in the cation sublattice, defects which may reduce gb conductivity and the support for a residual electronic conductivity, are investigated by optical spectroscopies.

3.4. Raman spectroscopy

Further insight into the structural characteristics of our $Li_{1+x}Cr_xTi_{2-x}(PO_4)_3$ samples was provided by micro-Raman spectra recorded both before and after annealing at 1000 °C. Raman spectra from different areas of the same sample were found to be identical, revealing the homogeneity of the investigated materials. The peak

Table 2
Activation energy, pre-exponential factor and ionic conductivity at room temperature in the bulk and grain boundaries obtained from Arrhenius fit.

	Bulk			Grain boundary		
	Ea (eV) ±0.02	σ_∞ (S cm^{-1}) ±30%	$\sigma_{(RT)}$ (S cm^{-1}) ±30%	Ea (eV) ±0.01	σ_∞ (S cm^{-1}) ±10%	$\sigma_{(RT)}$ (S cm^{-1}) ±10%
x = 0	0.67	163.3	$9.3\cdot10^{-10}$	0.81	223	$4.2\cdot10^{-12}$
x = 0.05	0.32	22.6	$8.0\cdot10^{-4}$	0.44	13.3	$4.7\cdot10^{-7}$
x = 0.1	0.31	19.2	$1.4\cdot10^{-4}$	0.39	10.1	$3.2\cdot10^{-6}$

positions of the observed bands and their corresponding assignments are shown in Table 3. Fig. 6 shows Raman spectra of the as-obtained powder samples. The frequency range has been divided in two intervals for comparison purposes.

The vibrational modes of LTP are usually divided into internal and external modes. Internal vibrations predominantly consist of intramolecular stretching and bending motions of the $(PO_4)^{3-}$ groups and can be described in terms of the fundamental vibrations of this free anion (ν_1–ν_4) [35–38]. Raman bands corresponding to stretching vibrations (ν_1 and ν_3) are observed above 950 cm^{-1}, while those corresponding to bending vibrations (ν_2 and ν_4) appear usually peaked between 420 and 650 cm^{-1}. The external modes (lattice phonon modes) are composed of Li^+, Ti^{4+} and $(PO_4)^{3-}$ translational vibrations, as well as librations (pseudo-rotations) of the $(PO_4)^{3-}$ anions [35–38]. Nevertheless, selection rules forbid Li^+ ion translation motions (frequently termed "cage modes") from being Raman active in LTP, since Li^+ ions occupy sites with S_6 symmetry [38]. External modes occur below ~350 cm^{-1} in the Raman spectra of $LiTi_2(PO_4)_3$. In general, it is rather difficult to assign a given frequency to a definite type of motion in this region of the spectrum, since the modes usually consist of mixtures of different types of atomic motions [35,36].

In the high frequency range [see Fig. 6(b)], the Raman spectra of our samples are dominated by two intense bands at 1095 and 1006 cm^{-1}. Two other bands appear peaked at 989 and 970 cm^{-1}, while two weak shoulders at about 1017 and 1072 cm^{-1} can be also discerned. Group theory predicts that ν_1 will yield two Raman active modes ($A_{1g} + E_g$), whereas ν_3 will give six Raman active vibrations ($A_{1g} + 2A_{2g} + 3E_g$) at the Brillouin zone center for $LiTi_2(PO_4)_3$ [35–38]. We attribute the bands observed at 989 and 970 cm^{-1} to symmetric stretching vibrations (ν_1) of the $(PO_4)^{3-}$ anions, and the peaks at 1095, 1072, 1017 and 1006 cm^{-1} to antisymmetric stretching vibrations (ν_3) of the same anions. Nevertheless, it should be mentioned that some authors [37] attribute the 1005 cm^{-1} band to the ν_1 mode based on its intensity and dominant character observed in their Raman spectra of $Li_xTi_2(PO_4)_3$ (x = 1,2,3). However, such assignments contradict the above-mentioned theoretical prediction and the experimental fact that symmetric stretching modes typically occur at lower frequencies than the antisymmetric modes [36,37].

Moreover, the band centered at about 1095 cm^{-1} is the dominant peak for all the samples investigated in this work, except for the undoped powder where its intensity is, nevertheless, comparable to the 1006 cm^{-1} peak. To the best of our knowledge, this has never been previously observed in Raman spectra of $M^IM^{IV}_2(PO_4)_3$ compounds (M^I = Li, Na, K, Rb, Cs; M^{IV} = Ge, Sn, Ti, Zr, Hf), where the 1095 cm^{-1} band is usually much weaker than the dominant Raman band centered near 1005 cm^{-1} [35–39]. In any case, it is not uncommon for distorted $(PO_4)^{3-}$ anions to produce ν_1 and ν_3 bands of comparable intensity, mainly due to the high electrical charge of PO_4 tetrahedra [39,40]. The

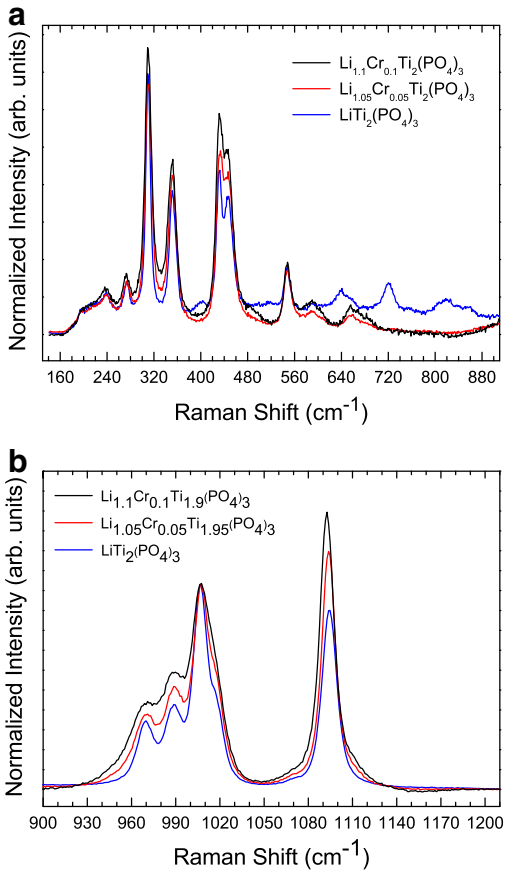

Fig. 6. Raman spectra of the undoped and Cr-doped as-obtained powders.

Table 3
Peak positions (cm^{-1}) of the observed Raman bands and proposed assignments.

x = 0 Powder	x = 0 Pellet	x = 0.05 Powder	x = 0.05 Pellet	x = 0.1 Powder	x = 0.1 Pellet	Assignment
1095	1095	1094	1094	1093	1093	ν_3 (PO_4)
1072	1071	1071	1071	1071	Not resolved	ν_3 (PO_4)
1017	1015	1018	1015	Not resolved	Not resolved	ν_3 (PO_4)
1006	1006	1007	1007	1007	1007	ν_3 (PO_4)
989	989	990	989	989	990	ν_1 (PO_4)
970	970	971	971	973	971	ν_1 (PO_4)
857	–	–	–	–	–	Li–O bond in $Li_{0.3}TiO_2$
720	–	–	–	–	–	P–O–P condensed phosphate groups
–	656	658	658	656	656	ν_4 (PO_4)
–	–	675	675	675	675	ν_4 (PO_4)
641	–	–	–	–	–	TiO_2 anatase
–	591	590	590	590	592	ν_4 (PO_4)
548	547	549	547	548	547	ν_4 (PO_4)
446	446	447	448	443	445	ν_2 (PO_4)
432	432	434	432	431	432	ν_2 (PO_4)
403	–	–	–	–	–	P–O bending in $Li(TiO)PO_4$
351	352	351	352	352	350	Ti–O vibration
309	309	310	310	309	310	Transl. + Librat. (PO_4)
273	274	274	274	273	273	Ti^{4+} translation
239	239	239	238	236	239	Transl. + Librat. (PO_4)
214	217	Not resolved	Not resolved	Not resolved	Not resolved	Transl. + Librat. (PO_4)
197	195	Not resolved	195	Not resolved	197	Transl. + Librat. (PO_4)

situation is further complicated because of possible mixing between ν_1 and ν_3 modes, which still remains an open question [35].

Raman spectra of $Li_{1+x}Cr_xTi_{2-x}(PO_4)_3$ between 850 and 145 cm^{-1} are shown in Fig. 6(a). The symmetric bending modes (ν_2) correspond to the bands peaked at 446 and 432 cm^{-1} [35–39], while the bands observed at 548, 591, 658 and 675 cm^{-1} are attributed to the symmetric bending motions (ν_4) of the $(PO_4)^{3-}$ anions [35–39], in agreement with factor group analysis that predicts four Raman active components for these vibrations [35].

As explained before, external modes appear below 350 cm^{-1} and their nature is difficult to ascertain. Some works report on the assignment of these bands through isotopic substitution studies or by comparing series of isostructural compounds [35,41]. Based on these and other investigations [39], the bands at 309, 239, 214 and 197 cm^{-1} can be assigned to translational and/or vibrational motions of the $(PO_4)^{3-}$ groups, the peak at 350 cm^{-1} is attributed to a Ti–O vibration mode [39] and the band at 273 cm^{-1} assigned to a translational vibration of the Ti^{4+} ions [38]. Other weak peaks, observed only in Raman spectra of the undoped powders, may not correspond to LTP vibrations but to minute amounts of second phases formed during the synthesis process and not detected by XRD measurements. The peak at 403 cm^{-1} was also observed by Cretin et al. [39] and attributed to an unidentified sub-product. A survey of the Raman spectra reported in the literature for possible second phases formed during the growth of our samples suggests that this band might be related to a P–O symmetric bending vibration in $Li(TiO)PO_4$ [42]. The peak at 720 cm^{-1} can be attributed to a (P–O–P) bending motion characteristic of condensed phosphate groups, such as $(P_2O_7)^{4-}$, or extended polyphosphate structures [38]. The disappearance of this band upon annealing at 1000 °C supports such assignment. The Raman peak at 857 cm^{-1} could be related to a stretching vibration of the shortest Li–O bond in $Li_{0.3}TiO_2$ [43]. Finally, the weak Raman band observed at about 640 cm^{-1} may indicate the presence of minute amounts of anatase TiO_2 [44].

The partial substitution of Ti^{4+} ions by Cr^{3+} ions does not significantly alter the positions of the above-mentioned Raman bands. However, some changes can be clearly appreciated in the width and relative intensity of several peaks. The intensity of the 1017 cm^{-1} band relative to the 1095 cm^{-1} band, decreases with increasing chromium content. There is still no definite explanation for such behavior, but a large influence of the cations on the Raman intensity of the (PO_4) anion in orthophosphates with NASICON-like structure has been previously reported [36]. In addition, a progressive broadening of vibration bands in the 920–1150 cm^{-1} range is observed when the chromium content is increased [Fig. 6(b)], evidencing a certain distortion or non-equivalency of vibrations of different $(PO_4)^{3-}$ groups due to the insertion of Cr^{3+} ions into the structure. A similar broadening was previously observed in Raman spectra of $Li_{1+x}Al_xTi_{2-x}(PO_4)_3$ [38] and $Li_{2x}Mn_{0.5-x}Ti_2(PO_4)_3$ [37] by respectively increasing the Al and Mn content. The increased lithium content associated to the higher chromium concentration may be also involved in the observed broadening, due to the establishment of static short range disorder associated to the filling of the available lithium sites [37]. In our case, this second mechanism seems to be more likely because of the similar ionic radius of Cr^{3+} (0.62 Å) and Ti^{4+} (0.61 Å).

3.5. Photoluminescence and cathodoluminescence spectroscopy

The influence of chromium content and thermal treatment on the luminescence properties of all the as grown powders and annealed pellets was studied by PL and CL spectroscopies. PL spectra of the $Li_{1+x}Cr_xTi_{2-x}(PO_4)_3$ powders are shown in Fig. 7(a), while PL spectra of the annealed pellets are shown in Fig. 7(b). The undoped material shows a complex PL emission in the visible range, centered near 526 nm (2.36 eV) with shoulders at about 419 nm (2.96 eV), 437 nm (2.84 eV) and 640 nm (1.94 eV). After annealing, the spectral distribution of the emission show only minor changes; it appears peaked at 521 nm (2.38 eV) and the intensity of the high wavelength shoulder is reduced. However, Cr incorporation strongly modifies the PL emission of the samples. The intensity of the blue–green luminescence decreases and new bands in the infrared spectral range become the dominant emissions. In the case of the $Li_{1.05}Cr_{0.05}Ti_{1.95}(PO_4)_3$ material, an asymmetric PL band peaked at 762 nm (1.63 eV) was found. Gaussian deconvolution (see Fig. 7(c)) reveals that two bands centered at 754 nm (1.64 eV) and 847 nm (1.46 eV) contribute to the observed emission. In the case of the $Li_{1.1}Cr_{0.1}Ti_{1.9}(PO_4)_3$ compound, a band at 875 nm (1.42 eV) shows

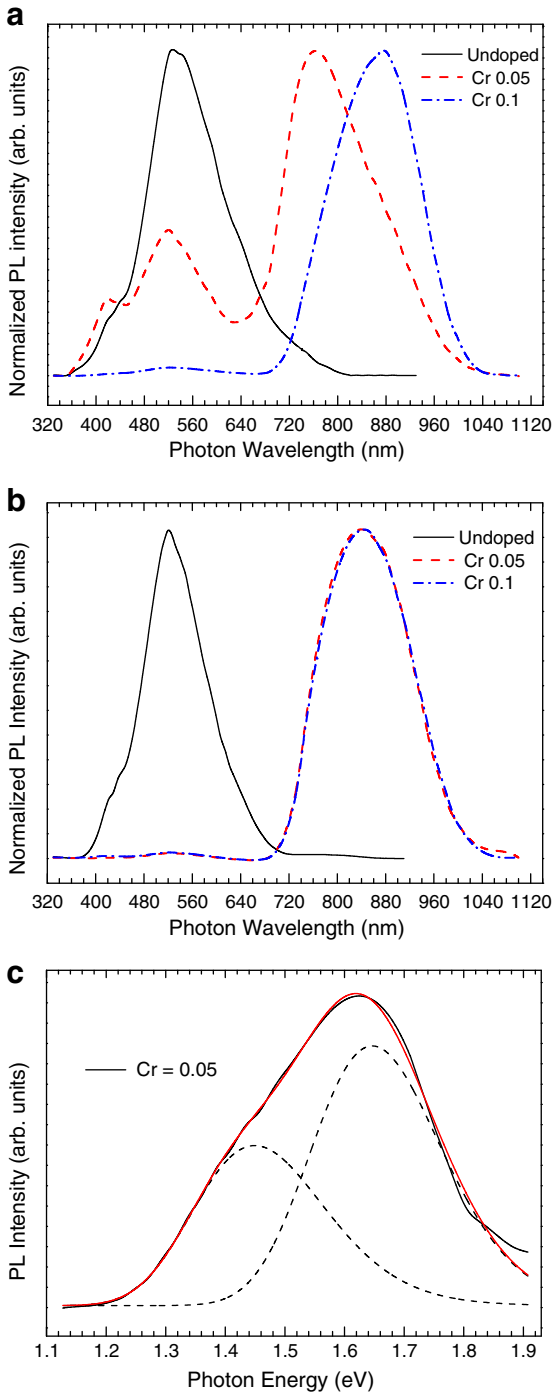

Fig. 7. PL spectra of the $Li_{1+x}Cr_xTi_{2-x}(PO_4)_3$ powders (a) and pellets (b). The Cr content is indicated in each graph. (c) Gaussian deconvolution of the PL spectrum of the $Li_{1.05}Cr_{0.05}Ti_{1.95}(PO_4)_3$ material. Emission bands are found centered at 1.64 and 1.46 eV (756 and 849 nm). The black solid line represents the experimental data while the red line corresponds to the best-fit curve.

the higher intensity in PL spectra. The doped annealed samples show identical PL spectral distribution. While the visible luminescence can be hardly observed, the strong and broad IR band peaked at 842 nm (1.47 eV) can be clearly appreciated.

Infrared emission was not observed in CL spectra of the samples investigated, irrespective of the Cr content or thermal treatments. CL spectra of the LTP powders recorded at different temperatures [Fig. 8(a)] appear peaked at 483 nm (2.56 eV), with clear shoulders at 532 nm (2.33 eV) and 380 nm (3.26 eV). The relative weight of this latter emission slightly increases by increasing temperature. CL spectra of the Cr-doped samples were found to be rather similar. Spectra of the $Li_{1.05}Cr_{0.05}Ti_{1.95}(PO_4)_3$ powders at different temperatures are shown in Fig. 8(b). The emission shows two peaks at 90 K, respectively centered at 478 nm (2.59 eV) and 437 nm (2.84 eV), with shoulders at 380 and 550 nm. The intensity of the emission decreases by increasing temperature and is almost quenched at about 260 K.

Emission bands in the visible range observed both in CL as in PL spectra from the undoped and chromium-doped samples is very close to that reported in previous works for TiO_2 and titanate micro and nanostructures [45–49]. Such bands appear peaked at about 380, 419, 437, 526 and 640 nm (3.26, 2.96, 2.84, 2.36 and 1.94 eV, respectively). Although the relative weight of these emissions depends on the excitation technique and the sample investigated, the obtained results strongly suggest that charge transfer transitions and/or oxygen related defects related to the TiO_6 octahedra are responsible for the observed luminescence [45–49], since these are the structural units common to all the mentioned materials. A clear example is shown in Fig. 9, that compares a PL spectrum of TiO_2 (anatase) material with the spectra of the undoped – both untreated and annealed – LTP samples, all of them recorded under the same experimental conditions. Luminescence at higher wavelengths is usually attributed to self-trapped excitons in the TiO_6 octahedra [46], while bands peaked between 450 and 650 nm have been associated with oxygen vacancies and related defects such as F centers [46] or electronic states bound to defects induced by coordinated groups on the surface [50]. Depending on their electronic charge, the related traps may act as radiative or non-radiative centers. According to different authors, the lower energy emissions would be related to oxygen vacancies [45], while PL bands centered near 483 and 525 nm have been respectively associated to surface F and F^+ centers in anatase TiO_2 nanowires [46]. Annealing in air at 1000 °C decreases both the surface state density and the concentration of oxygen vacancies, which results in the decrease of the visible luminescence intensity.

The PL band centered at about 754 nm in the $Li_{1.05}Cr_{0.05}Ti_{1.95}(PO_4)_3$ sample (see Fig. 7) can be attributed to $^4T_2 \rightarrow {}^4A_2$ intraionic transitions of Cr^{3+} ions in octahedral coordination [51–54]. This is a spin-allowed, parity forbidden, transition that can be partially allowed by a weak distortion of the crystal field or by instantaneous distortions due to molecular vibrations [52]. The width of the associated PL emission implies strong electronic coupling to vibrations of the local environment. The appearance of this band and the absence of the so-called R lines, usually observed as sharp emissions peaked between 690 and 700 nm, indicate that Cr^{3+} ions occupy low crystal field sites, in which the $^4T_2$ levels lie below the ^2E level [51]. This PL emission is quenched when the Cr content increases or the obtained materials are annealed at 1000 °C, probably due to a concentration quenching effect [55], meaning that the intensity of the ion luminescence decreases with increasing ion concentration. This effect dominates if the excitation energy is transferred between many ions in the time necessary for the radiative decay, frequently called energy transfer. In such a situation, the probability to reach a path of non-radiative decay is strongly enhanced. The energy transfer probability is increased with decreasing ion distance, *i.e.*, increasing the ion concentration. Moreover, such emission is not observed in CL spectra. This can be attributed to a number of factors, including charge trapping and electron beam local heating. Actually, thermally assisted non-radiative decay of $^4T_2 \rightarrow {}^4A_2$ intraionic transitions is favored for weak crystal fields [53]. Some authors [56] have also considered the possibility of P^{5+} substitution in double phosphate crystals by Cr^{6+} ions, with the resulting formation of deformed CrO_4 tetrahedra containing $(CrO_4)^{2-}$ groups. This possibility can be ruled out in the present case, since the weak luminescence of $(CrO_4)^{2-}$ groups appears peaked between 625 and 670 nm approximately [57].

The infrared photoluminescence peaked between 842 nm and 875 nm is not related to Cr ions, but to $^2T_{2g} \rightarrow {}^2E_g$ intraionic transitions of Ti^{3+} ions in octahedral coordination. Similar emission bands have been reported in different samples containing TiO_6 structural units (as TiO_2) or doped with Ti atoms [37,39,58]. The width of the observed band reveals a certain distortion of the TiO_6 octahedra that may be in turn attributed to the effect of disordered phosphate groups, in agreement

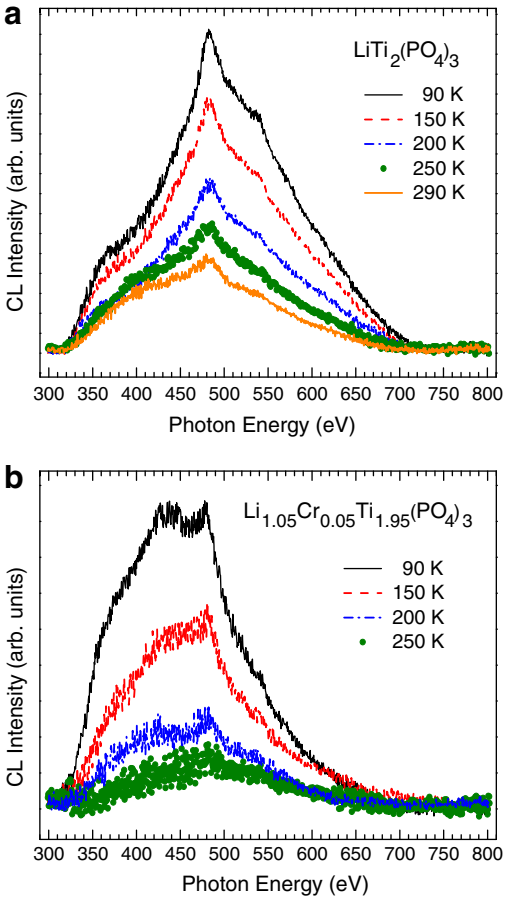

Fig. 8. (a) $LiTi_2(PO_4)_3$ and (b) $Li_{1.05}Cr_{0.05}Ti_{1.95}(PO_4)_3$ powder materials CL spectra recorded at temperatures 90–290 K from top to bottom.

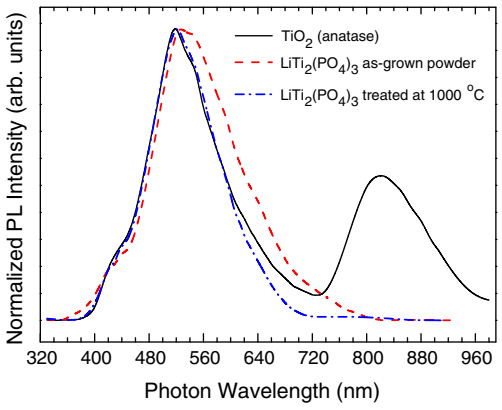

Fig. 9. PL spectra of anatase TiO_2 powder, untreated and annealed $LiTi_2(PO_4)_3$ samples.

with our Raman results. The PL spectrum of anatase TiO_2 powder shown in Fig. 9, where the Ti^{3+} emission appears centered at 824 nm (1.50 eV), supports this assignment. Although this result confirms that Cr^{3+} intraionic transitions are not responsible for the long wavelength IR emission, the increase of Cr concentration enhances the mentioned luminescence. This can be tentatively attributed to an increased oxygen vacancy concentration, as previously reported for Cr-doped TiO_2 [59,60]. The two electrons left by the removed oxygen atom migrate into the conduction band, the bottom of which consists of Ti 3d states [61]. Both Ti atoms surrounding the removed oxygen atom capture an electron, increasing the number of Ti^{3+} ions. This electronic doping supports the existence of a residual electronic conductivity, as indicated in the dielectric spectroscopy experiments.

Besides, annealing at 1000 °C also enhances the 880 nm PL. An increase of the intensity of the Ti^{3+} luminescence together with a strong reduction of the visible emission has been observed in TiO_2 annealed at 980 °C and attributed to grain growth and faceting [47]. In the present case, SEM images of the chromium-doped samples annealed at 1000 °C (Fig. 2) reveal a sintered polycrystalline material with grains of about (400–600) nm in size showing well-defined faces, while the average grain size of the untreated samples is much smaller. This observation supports the possibility that the enhancement of the 880 nm IR luminescence may be related to an increased grain size, as proposed for titania ceramics.

4. Conclusions

Materials with $Li_{1+x}Cr_xTi_{2-x}(PO_4)_3$ ($x = 0, 0.05$ and 0.1) composition have been prepared as pure rombohedral Nasicon-type phases by the Pechini sol-gel synthesis method and the effect of chromium content on their optical and electrical properties has been studied. Dielectric spectroscopy evidences an enhanced ionic conductivity even for the addition of small amounts of Cr. We interpret this conductivity increase as a consequence of an enhanced lithium mobility due to the release of the bottleneck M1 positions of the Nasicon structure promoted by Cr insertion, resulting in a reduction of the activation energy. A room-temperature conductivity of $1.4 \cdot 10^{-4}$ S cm^{-1} and an activation energy of 0.31 eV were obtained for $x = 0.1$ sample, which are comparable to those of the best ionic conductors reported to date. The ionic conductivity across grain boundaries correlates with the increased density of the pellets that takes place upon Cr addition, as revealed by SEM images. A residual electronic contribution to the conductivity is indicated in the doped samples, at similar level as the grain boundary undoped sample, but different activation energy.

The insertion of chromium gives rise to a progressive broadening of several vibration bands in the Raman spectra due to a static short range disorder associated to lithium ions, correlated to the delocalization of lithium ions within the crystal structure. PL and CL spectroscopies showed that self-trapped excitons and oxygen defects related to the TiO_6 octahedra are responsible for the observed luminescence in the visible spectral range. Oxygen vacancies appear to be involved in the residual electronic conductivity found in the dielectric spectroscopy experiments. Cr incorporation strongly modifies the PL emission of the samples, giving rise to IR emission bands that can be attributed to different Cr^{3+} and Ti^{3+} intraionic transitions. Cr incorporation thus modifies the defect structure of the investigated phosphates that correlates with an increase in the grain boundary ionic conductivity. Systematic studies in different doped materials should elucidate the generality of the present results.

Acknowledgments

This work has been supported by MICNN through projects MAT2009-07882 and CSD2009-0013 and by UCM-BSCH (GR58-08-910072, GR35-10A-910146, GR42/10962045 and G79485082). The authors also acknowledge the Neurociencias y Envejecimiento Foundation for its financial support.

References

[1] E. Quartarone, P. Mustarelli, Chem. Soc. Rev. 40 (2011) 2525–2540.
[2] M. Park, X. Zhang, M. Chung, G.B. Less, A.M. Sastry, J. Power Sources 195 (2010) 7904–7929.
[3] V. Thangadurai, W. Weppner, Ionics 12 (2006) 81–92;
K. Nagata, T. Nanno, J. Power Sources 174 (2007) 832–837.
[4] X. Xu, Z. Wen, X. Yang, J. Zhang, Z. Gu, Solid State Ionics 177 (2006) 2611–2615.
[5] J.S. Thokchom, B. Kumar, Solid State Ionics 177 (2006) 727–732.
[6] J. Santos-Peña, M. Cruz-Yusta, P. Soudan, S. Franger, J.J. Cuart-Pascual, Solid State Ionics 177 (2006) 2667–2674.
[7] M. Barré, M.P. Crosnier-López, F. LeBerre, E. Suard, J.L. Fourquet, J. Sol. State Chem. 188 (2007) 1011–1019.
[8] P. Gibot, M. Casas-Cabanas, L. Laffont, S. Levasseur, P. Carlach, S. Hamelet, J.M. Tarascon, C. Masquelier, Nat. Mater. 7 (2008) 741–747.
[9] P. Knauth, Solid State Ionics 180 (2009) 911–916.
[10] M.A. París, A. Martínez-Juarez, J.M. Rojo, J. Sanz, J. Phys. Condens. Matter 8 (1996) 5355–5366.
[11] H. Aono, E. Sugimoto, Y. Sadaoka, N. Imanaka, G. Adachi, Chem. Lett. 28 (1990) 1825–1828.
[12] H. Aono, E. Sugimoto, Solid State Ionics 40 (41) (1990) 38–42.
[13] H. Aono, E. Sugimoto, Y. Sadaoka, N. Imanaka, G. Adachi, Solid State Ionics 47 (1991) 257–264.
[14] K. Arbi, S. Mandal, J.M. Rojo, J. Sanz, Chem. Mater. 14 (2002) 1091–1097;
K. Arbi, J.M. Rojo, J. Sanz, J. Eur. Ceram. Soc. 27 (2007) 4215–4218.
[15] K. Arbi, M. Tabellout, M.G. Lazarraga, J.M. Rojo, J. Sanz, Phys. Rev. B 72 (2005) 094302–094309.
[16] P. Maldonado-Manso, M.C. Martín-Sedeño, S. Bruque, Solid State Ionics 178 (2007) 43–52.
[17] A.S. Best, M. Foryth, D.R. Mac Farlane, Solid State Ionics 136 (2000) 339–344.
[18] G. Nuspl, T. Takeuchi, A. Weiβ, H. Kageyama, K. Yoshizawa, T. Yamabe, J. Appl. Phys. 86 (1999) 5484–5491.
[19] Y. Shimizy, Y. Azuma, S. Michishita, J. Mater. Chem. 7 (1997) 1487–1490.
[20] M. Cretin, P. Fabry, J. Eur. Ceram. Soc. 19 (1999) 2931–2940.
[21] X.M. Wu, X.H. Li, S.W. Wang, Z. Wang, Y.H. Zhang, M.F. Xu, Z.Q. He, Thin Solid Films 425 (2003) 103–107.
[22] J.L. Narváez-Semanate, A.C.M. Rodrigues, Solid State Ionics 181 (2010) 1197–1204.
[23] Z. Lin, H. Yu, S. Li, S. Tian, Solid State Ionics 31 (1988) 91–94.
[24] M.P. Pechini, USA Num 3: 330 (11–07–1967).
[25] H. Aono, E. Sugimoto, J. Electrochem. Soc. 137 (1990) 1023–1027.
[26] R. Ramaraghavulu, S. Buddhudu, Ceram. Int. 37 (2011) 3651–3656.
[27] T. Roisnel, J. Rodriguez-Carvajal, WinPLOTR, http://www-llb.cea.fr/fullweb/winplotr/winplotr.htm.
[28] A. Rivera, T. Blochowicz, C. Gainaru, E.A. Roessler, J. Appl. Phys. 96 (2004) 5607–5612.
[29] J.R. Mcdonald, Impedance Spectroscopy, John Wiley and Sons, 1987.
[30] K. Takada, M. Tansho, I. Yanase, T. Inada, A. Kajiyama, M. Kouguchi, S. Kondo, M. Watanabe, Solid State Ionics 139 (2001) 241–247.
[31] F.E. Mouahid, M. Zahir, P. Maldonado-Manso, S. Bruque, E.R. Losilla, M.A.G. Aranda, A. Rivera, C. León, J. Santamaría, J. Mater. Chem. 11 (2001) 3258–3563.
[32] M. Catti, A. Comotti, S. Di Blas, R.M. Ibberson, J. Mater. Chem. 14 (2004) 835–839.
[33] A. Rivera, C. León, J. Santamaría, A. Varez, O. V'yunov, A.G. Belous, J.A. Alonso, J. Sanz, Chem. Mater. 14 (2002) 5148–5152.
[34] J. Garcia-Barriocanal, A. Rivera-Calzada, M. Varela, Z. Sefrioui, E. Iborra, C. Leon, S.J. Pennycook, J. Santamaria, Science 324 (2009) 1169018.
[35] P. Tarte, A. Rulmont, C. Merckaert-Ansay, Spectrochim. Acta 42A (1986) 1009–1016.
[36] M. Barj, G. Lucazeu, C. Delmas, J. Solid State Chem. 100 (1992) 141–150.
[37] R. Pikl, D. de Waal, A. Aatiq, A. el Jazouli, Mater. Res. Bull. 33 (1998) 955–961.
[38] C.M. Burba, R. French, Solid State Ionics 177 (2006) 1489–1494.
[39] M. Cretin, P. Fabry, L. Abello, J. Eur. Ceram. Soc. 15 (1995) 1149–1156.
[40] C.M. Burba, R. French, J. Electrochem. Soc. 151 (2004) 1032–1038.
[41] V.V. Kravchenko, V.I. Michailov, S.E. Segaryov, Solid State Ionics 50 (1992) 19–30.
[42] M. Chakir, A. El Jazouli, J.P. Chaminade, F. Bouree, D. de Waal, J. Solid State Chem. 179 (2006) 18–28.
[43] M. Smirnov, R. Baddour-Hadjean, J. Chem. Phys. 121 (2004) 2348–2355.
[44] T. Ohsaka, F. Izumi, Y. Fujiki, J. Raman Spectrosc. 7 (1978) 321–324.
[45] T. Sekiya, S. Kamei, S. Kurita, J. Lumin. 87–89 (2000) 1140–1142.
[46] J.M. Wu, H.C. Shih, W. Wu, Y. Tseng, I. Chen, J. Cryst. Growth 281 (2005) 384–390.
[47] D. Maestre, A. Cremades, J. Piqueras, Nanotechnology 17 (2006) 1584–1588.
[48] G. Blasse, G.J. Dirksen, Chem. Phys. Lett. 62 (1979) 19–20.
[49] C. Díaz-Guerra, P. Umek, A. Glotter, J. Piqueras, J. Phys. Chem. C 114 (2010) 8192–8198.
[50] Y.C. Zhu, C.X. Ding, J. Solid State Chem. 145 (1999) 711–715.
[51] F. Rasheed, K.P. O'Donnell, B. Henderson, D.B. Hollis, J. Phys. Condens. Matter 3 (1991) 1915–1930.
[52] M. Haouari, M. Ajroud, H. Ben Ouada, H. Maaref, A. Brenier, C. Garapon, Phys. Status Solidi B 215 (1999) 1165–1177.
[53] F. Rasheed, K.P. O'Donnell, B. Henderson, D.B. Hollis, J. Phys. Condens. Matter 3 (1991) 3825–3840.
[54] T.P.J. Han, F. Jaque, V. Bermúdez, E. Diéguez, Chem. Phys. Lett. 369 (2003) 519–524.

[55] G. Boulon, in: C. Webb, J. Jones (Eds.), Handbook of Laser Technology and Applications, vol. II, IOP Publishing Ltd., Bristol, UK, 2004, pp. 307–338.
[56] O.V. Gomenyuk, S.G. Nedilko, N.V. Stus, M.S. Slobodyanyk, V.P. Scherbatsky, Funct. Mater. 11 (2004) 153.
[57] G.A.M. Dalhoeven, G. Blasse, Chem. Phys. Lett. 76 (1980) 27–29.
[58] L.E. Bausa, F. Jaque, J. García Solé, R. Cases, A. Durán, J. Lumin. 40–41 (1988) 193–194.
[59] D.E. Williams, P.T. Moseley, J. Mater. Chem. 1 (1991) 809–814.
[60] U. Kirner, K.D. Schierbaum, W. Gopel, B. Leibold, N. Nocoloso, W. Weppner, D. Fischer, W.F. Chu, Sens. Actuators B 1 (1990) 103–107.
[61] S. Nedilko, Yu. Hizhnyi, O. Chukova, P. Nagornyi, R. Bojko, V. Boyko, J. Nucl. Mater. 385 (2009) 479–484.